Realization of extreme nonstoichiometry in gadolinium aluminate garnet phosphors by nonequilibrium synthesis

Xue Fang[1]†, Victor Castaing[2], Ana Isabel Becerro[2], Weiwei Cao[1], Emmanuel Veron[1], Didier Zanghi[1], Matthew S. Dyer[3], Cécile Genevois[1], Mathieu Allix[1]* and Michael J. Pitcher[1]*

[1]CNRS, UPR3079 CEMHTI, 1D avenue de la Recherche Scientifique, 45071 Orléans, France
[2]Instituto de Ciencia de Materiales de Sevilla (CSIC-US), c/Américo Vespucio, 49, 41092 Seville, Spain
[3]Department of Chemistry, University of Liverpool, Crown Street, Liverpool L69 7ZD, UK

†*Current address*: Advanced Energy Storage Technology Research Center, Shenzhen Institute of Advanced Technology, Chinese Academy of Sciences, Shenzhen 518055, China

Email: mathieu.allix@cnrs-orleans.fr, michael.pitcher@cnrs-orleans.fr

Abstract

Rare-earth aluminates with the garnet structure represent an important class of optical materials with a range of applications. When synthesized as ceramics or single crystals, these materials do not tolerate large deviations from ideal $RE_3Al_5O_{12}$ stoichiometry, and their luminescence properties are typically controlled by dopant selection. Here, we use glass crystallization as a nonequilibrium synthesis route to a new family of highly nonstoichiometric gadolinium aluminate garnet (GAG) phosphor hosts $Gd_{3+x}Al_{5-x}O_{12}$ with $0 \leq x \leq 0.60$. In these materials, excess Gd^{3+} is accommodated on the octahedrally-coordinated Al^{3+} sublattice of the garnet structure. The endmember $Gd_{3.6}Al_{4.4}O_{12}$ has 30% of these Al^{3+} sites substituted by Gd^{3+}, but retains the garnet structure despite the vast size contrast between the two cations. The nonstoichiometry range for GAG extends far beyond that of nonstoichiometric YAGs ($Y_{3+x}Al_{5-x}O_{12}$, $0 \leq x \leq 0.4$), enabled by a broader glass-forming domain in the $Gd_2O_3 – Al_2O_3$ system. We investigate three model phosphor systems based on GAG, and determine the crystallographic distributions of the dopant ions where possible, to evaluate the response of upconversion and photoluminescence to extreme nonstoichiometry. In particular, upconversion from the small rare-earth activator Tm^{3+} is found to be sensitive to nonstoichiometry in GAG. These results demonstrate that highly nonstoichiometric garnet aluminates are not limited to small rare-earth hosts such as YAG and should be realizable from Gd - Lu, highlighting the potential for color tuning of new upconversion phosphors by control of host stoichiometry and opening new opportunities for development of different garnet-based optical and magnetic materials.

1. Introduction

The rare-earth aluminate garnets $RE_3Al_5O_{12}$ (*RE* = Eu – Lu, Y) are attractive host materials for optical applications in solid state lasers,[1] lighting and display technologies[2] and scintillation detectors[3], owing to their excellent optical isotropy, chemical and physical stability, and their crystal structure exhibiting three types of cationic environments suitable for doping with different emission centres. These materials form over extremely narrow compositional ranges, typically represented as line phases in the RE_2O_3 – Al_2O_3 pseudo-binary phase equilibria diagrams. This characteristic is rooted in their crystal chemistry: their structures (general formula $A_3B_2C_3O_{12}$) feature three cation sublattices *A* (8-coordinate dodecahedral site), *B* (6-coordinate octahedral) and *C* (4-coordinate tetrahedral), shown in Figure 1. The resulting segregation of large RE^{3+} and small Al^{3+} onto the *A* and (*B*, *C*) sublattices respectively is associated with a low tolerance to deviation from ideal (3:5) stoichiometry. For example, in $Y_3Al_5O_{12}$ (YAG), the most energetically favourable way to deviate from the nominal stoichiometry is to substitute Y^{3+} for *B* site Al^{3+},[4] but such substitutions are difficult to realise in appreciable concentrations, with an estimated limit of $x < 0.03$ in conventionally-synthesised YAG ceramics.[5] This behavior is common to all members of the $RE_3Al_5O_{12}$ series[6] and means that rare-earth dopants used to introduce and control luminescence properties are effectively constrained to a single crystallographic sublattice (*A*) with similar local coordination environments around each dopant ion. The luminescence properties of the phosphors are thus controlled by the identity of the dopant(s), with little scope for further property tuning via control of dopant distribution within the host structure. However, if large deviations from 3:5 stoichiometry can be imposed on the host structure, it becomes possible to distribute significant concentrations of dopant ions over multiple cation sublattices, representing an extra degree of freedom for property tuning. We recently demonstrated this effect in a series of highly nonstoichiometric YAGs ($Y_{3+x}Al_{5-x}O_{12}$ with $0 \leq x \leq 0.40$),[7] which can be isolated by crystallisation of glass or deeply-undercooled melts. In these materials, excess Y^{3+} is accommodated by substituting up to 20% of the Al^{3+} at the *B* sublattice. This allows small RE^{3+} dopants such as Yb^{3+} and Er^{3+} to be distributed over the *A* and *B* sublattices, with a strong effect on the color of their upconversion emission.

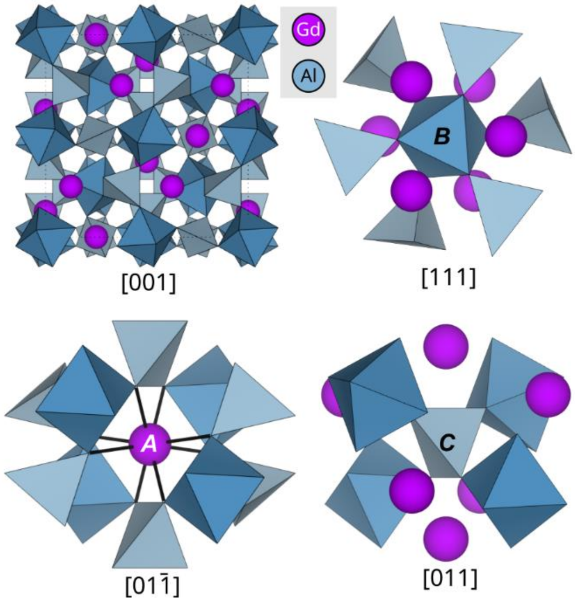

Figure 1. Unit cell of the cubic garnet structure of $Gd_3Al_5O_{12}$ projected along [001] (cell edges marked by dashed line), with structural fragments showing the local *A*, *B* and *C* cation environments.

The extension of this concept to non-YAG garnets ($RE_{3+x}Al_{5-x}O_{12}$) could have significant advantages, but it also presents certain challenges. Notably, a wider range of applications can be addressed by changing RE^{3+}. For example, as well as their luminescence properties (that are complementary to those of YAG), $RE_3Al_5O_{12}$ garnet aluminates based on heavier rare-earths such as $Lu_3Al_5O_{12}$ are particularly suitable for use as scintillators;[3] while the $Gd_3Al_{5-x}Ga_xO_{12}$ family hosts excellent persistent luminescence properties;[8,9] and the various open-shell $4f^x$ configurations support different magnetic phenomena and applications.[10–12] The challenges to this development relate mainly to synthesis and crystal chemistry: the extent of crystallographic site-sharing between Al^{3+} and Y^{3+} in $Y_{3+x}Al_{5-x}O_{12}$ is already surprising due to their large size contrast,[7] but several of the garnet-forming rare earth ions have an even larger radius than yttrium. Conventional crystallo-chemical assumptions suggest that these should be even less amenable to non-stoichiometry. Like YAG, nonstoichiometric $RE_{3+x}Al_{5-x}O_{12}$ are expected to be metastable, and should require an appropriate synthesis route that avoids extended annealing times at very high temperatures. It is clear that, before the potential of $RE_{3+x}Al_{5-x}O_{12}$ functional materials can be realized, it is important to understand which RE^{3+} systems are amenable to extreme nonstoichiometry, where their compositional and thermal stability limits lie, and how to synthesize them.

Here, we focus on *RE* = Gd^{3+} (GAG), which has been investigated extensively for its optical properties including luminescence and scintillation,[13,14] and for its complex low temperature magnetism.[10,11] $Gd_3Al_5O_{12}$ lies close to the stability limit of the $RE_3Al_5O_{12}$ series (*RE* = Eu – Lu, Y) and is itself metastable,[15] but it is readily synthesised in polycrystalline form by sol-gel[16] and glass crystallisation[7,17] methods. Polycrystalline GAG-based phosphors are more easily prepared when the garnet phase is stabilised by substituents that reduce the A/(B,C) ionic radius ratio (e.g. Lu^{3+} for Gd^{3+}; Ga^{3+} for Al^{3+}).[18,19] The substitution of Gd^{3+} by larger RE^{3+} ions increases this ratio and rapidly destabilises the garnet structure: $Eu_3Al_5O_{12}$ is significantly more challenging to synthesise,[20] and to the best of our knowledge there are no reports of bulk $Sm_3Al_5O_{12}$. As Gd^{3+} is the largest RE^{3+} ion to yield a readily-synthesisable $RE_3Al_5O_{12}$ garnet, compared to YAG, it may be possible to distribute a wider range of RE^{3+} dopants over multiple sublattices due to the larger *B* site environment induced by nonstoichiometry in a $Gd_{3+x}Al_{5-x}O_{12}$ system. Here, we explore the compositional limits of the highly nonstoichiometric GAG system $Gd_{3+x}Al_{5-x}O_{12}$ synthesised by glass crystallization, and investigate experimentally the structural and luminescence responses of three different phosphor types (upconversion and broad-/narrow-band photoluminescence) to nonstoichiometry.

2. Experimental

2.1 Crystallization from glass synthesis

High purity commercial starting chemicals Gd_2O_3 (Strem, 99.99%), Al_2O_3 (Strem, 99.999%), CeO_2 (Alfa Aesar 99.99%), Tb_2O_3 (Strem, 99.999%), Tm_2O_3 (Strem, 99.95%) or Yb_2O_3 (Strem, 99.9%) were weighed according to the chemical formula and mixed well with ethanol in an agate mortar. The dried mixed powders were pelletized with a uniaxial press, then broken into fragments of approximately 50 mg. Individual fragments were loaded into the nozzle of an aerodynamic levitation furnace (see Supporting Information S1). An oxygen gas jet was used to levitate the samples, and a pair of CO_2 lasers were used to heat them, with temperatures monitored by an optical pyrometer. Melting occurred at approximately 1800°C for all samples. The levitating melts were then held for a few seconds at ~2200°C, then quenched rapidly to ambient temperature by switching off the lasers, to yield transparent glass beads of ~2 mm diameter. The formation of glass was verified by PXRD of crushed beads, which showed no Bragg peaks. The glass-transition and crystallization temperatures were determined by differential scanning calorimetry. Crystallization was induced by heating glass powders or beads in a muffle furnace at 950°C in air for 3 hours, or for the same temperature and time in a reducing environment (5%H_2 and 95% argon gas flow) for the Ce^{3+}-doped series $(Gd_{0.98}Ce_{0.02})_{3+x}Al_{5-x}O_{12}$.

2.2 Characterization

X-ray diffraction: Powder X-ray diffraction (PXRD) patterns were recorded from 10 to 80° (2θ) with a step size of 0.02° and a scan time of 2s per step using a D8 Advance Bruker diffractometer (Cu $K\alpha_{1,2}$ radiation, LynxEye detector) at room temperature in Bragg-Brentano geometry. Finely-ground powder samples were dispersed on silicon wafers from an ethanol mull. In situ variable temperature diffraction (VT-XRD) data were collected using a Bruker D8 Advance diffractometer (Cu$K\alpha_{1,2}$ radiation, Vantec detector) equipped with an HTK1600N Anton Paar furnace. Powder samples were deposited on a platinum ribbon from an ethanol mull, and measurements were collected in Bragg-Brentano geometry with the sample under vacuum, from room temperature up to 1600°C in the 2θ range 10-120° with a step size of 0.02° and a scan time of 2s per step. High-resolution synchrotron powder diffraction (SPD) data were recorded on 11-BM diffractometer at Argonne National Laboratory, U.S.A. in the range of 2θ from 1 ° to 50° with a 0.0001° step size using a wavelength of 0.4578 Å at room temperature. The measured powders were obtained by crushing one bead for each composition and loading into glass capillaries with a diameter of 0.3 - 0.5mm. Rietveld refinements were performed using TOPAS Academic version 6.[21]

Thermal analysis: Differential scanning calorimetry (DSC) data were acquired on heating using a Perkin Elmer Setaram MULTI HTC 1600 Thermal Analyzer with a heating rate of 10 $°C.min^{-1}$ under a constant argon flow (20 cm^3 min^{-1}). Experiments were conducted on glass powders contained in a platinum vessel, except for x=0.6 which was conducted on a bulk (single bead) sample.

SEM and microprobe: An IT800SHL JEOL scanning electron microscope (FEG SEM) equipped with an SSD Ultim Max 100mm2 detector (EDS Oxford system) was used for microstructural analysis. High precision elemental analysis was examined by using a Cameca SX Five electron microprobe (EMP) (40 points per sample). All samples for SEM imaging and microprobe testing were obtained from randomly selected crystallized beads embedded in epoxy resin, polished and carbon coated under vacuum.

EXAFS: X-ray absorption fine structure (EXAFS) spectra were recorded at the Gd L_3-edge (7243 eV), Tm

L_3-edge (8648 eV) and Yb L_3-edge (8944 eV) using the SAMBA beamline (SOLEIL synchrotron, France). Samples were diluted with BN to give suitable absorption rates (concentrations calculated using MAX[22]) and pressed into pellets of 10 or 13 mm diameter. Spectra were recorded in transmission mode at ambient temperature using a Si (220) monochromator with ionization chamber detectors. For each pellet, several zones were sampled using 3 x 0.25 mm incident beam, and these were summed to produce the final spectra for analysis. Gd_2O_3, Tm_2O_3 and Yb_2O_3 were used as standards. The first coordination sphere Gd-O and Tm(Yb)-O distances were extracted by fitting each spectrum to a 1 x 1 x 1 garnet unit cell using FASTOSH[23] and FEFF8[24] to a limit of 5 Å. To support this analysis, structural models were generated from a 1 x 1 x 1 $Gd_3Al_5O_{12}$ unit cell (160 atoms; *P*1) by substituting 0, 1, 2 or 3 Gd^{3+} ions for Al^{3+} at the *B* sublattice (corresponding to $x = 0$, 0.125, 0.25 or 0.375), and 0, 1 or 2 Tm $(Yb)^{3+}$ ions at the *A* and/or *B* sublattices (corresponding to dopant concentrations of 0, 4 or 8 %). For each composition, all symmetrically-inequivalent structural configurations were generated using Supercell.[25] Due to the large number of inequivalent configurations for highly nonstoichiometric Tm(Yb)-doped compositions (e.g. 453 unique configurations for $x = 0.25$ with 8% Tm doping), a small number of representative configurations from each composition were selected for relaxation via plane-wave based DFT calculations using VASP.[26] These used the PBEsol functional[27] with the projector augmented wave method[28] for the treatment of core electrons. Structures were optimized with a 600 eV plane-wave cutoff and a 5×5×5 *k*-point grid until forces fell below 10^{-3} eV Å^{-1}.

Luminescence: Photoluminescence (PL), upconversion (UC), and photoluminescence excitation (PLE) spectra of samples at room temperature were recorded using an FLS1000 photoluminescence spectrometer (Edinburgh Instruments) equipped with a 980 nm laser (2 W of optical power) and a Xe-lamp as excitation sources. The luminescence decay curves of UC phosphors were measured in the same instrument at room temperature under excitation by the 980 nm laser in pulsed mode. The dependence of the peak intensity of UC luminescence was recorded by varying the pump power of the 980 nm laser using an iris filter. All samples tested were placed in a fused silica sample holder. The disk-shaped samples used for PL and UC measurements were obtained from crystallized beads by polishing two parallel faces.

3. Results

3.1 Synthesis conditions for nonstoichiometric $Gd_{3+x}Al_{5-x}O_{12}$ (GAG)

Rapid quenching of aerodynamically levitated melts was used to synthesize a range of $Gd_{3+x}Al_{5-x}O_{12}$ precursor glasses with nominal compositions $0 \leq x \leq 0.7$. For all compositions, transparent glass beads were obtained most reliably by using an oxygen gas jet, which affords a faster cooling rate than levitation in argon[10]. A representative cooling curve for the formation of $Gd_{3.2}Al_{4.8}O_{12}$ glass in an oxygen gas jet is shown in Figure 2a, with a photograph (inset) of a typical glass bead. The slower cooling rates afforded by quenching in an argon jet produced fully-crystallized opaque beads with perovskite ($GdAlO_3$) as the majority phase (see Supporting Information S2). We did not observe any intermediate quenching conditions that lead consistently to direct crystallization of garnet on quenching (in contrast to the YAG system where such a mechanism is readily accessed[7]). The glass transition and crystallization temperatures of 850(2) and 925(2) °C respectively were extracted from DSC curves (see Figure 2b, and Supporting Information S4-S8). With the exception of $x = 0.7$ (see section 3.2), the glass beads crystallized fully into the garnet structure after heating for three hours in a muffle furnace at 950°C, as shown by the PXRD patterns in Figure 2c, and had typical ceramic-type microstructures with no apparent residual glass at the micron scale (see Supporting Information S12). The crystallization step causes a loss of bead transparency (see Figure 2(b) inset): this is typical behavior for garnet vitroceramics, where large differences in density between glass and crystalline states cause fractures and pores to form upon crystallization.[29] For compositions $0 \leq x \leq 0.5$, the same crystallization products were obtained from powders and as-made beads, suggesting that surface crystallization is not dominant in this system. For compositions $x > 0.5$, high quality garnet samples could only be obtained by crystallizing bulk beads rather than powders, due to competition from surface crystallization of perovskite.

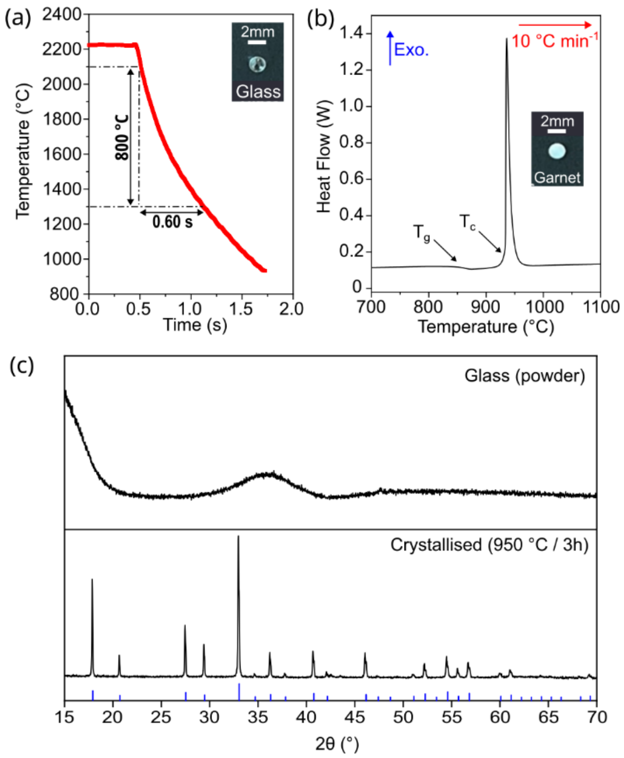

Figure 2. Synthesis of $Gd_{3.2}Al_{4.8}O_{12}$ by glass crystallization. (a) Temperature profile of a $Gd_{3.2}Al_{4.8}O_{12}$ melt free-cooled in an oxygen jet, resulting in a glass bead (see photograph, inset). (b) DSC scan recorded on $Gd_{3.2}Al_{4.8}O_{12}$ glass powder (crushed beads) on heating at 10 °C min^{-1}, showing a glass transition (T_g) at ~850 °C and the onset of crystallization (T_c) at ~925 °C. Inset, photograph of a crystallized $Gd_{3.2}Al_{4.8}O_{12}$ bead. (c) Laboratory PXRD scans of glass powder before (upper panel) and after (lower panel) thermal treatment at 950°C for 3 hours, with the crystalline phase indexed to a cubic garnet structure (blue stick diagram, base of frame).

3.2 Crystal structures of nonstoichiometric $Gd_{3+x}Al_{5-x}O_{12}$

The laboratory PXRD patterns of $Gd_{3+x}Al_{5-x}O_{12}$ with nominal compositions $0 \le x \le 0.6$, after crystallization, are shown in Figure 3. The patterns from $0 \le x \le 0.5$ are phase-pure with a cubic garnet as the sole crystalline phase. The patterns of $x = 0.55$ and 0.60 are dominated by the same cubic garnet, but contain a set of weak Bragg peaks corresponding to a perovskite impurity phase ($GdAlO_3$), with the $x = 0.6$ member containing 16.3(9) wt.% of this phase. An abrupt change was observed at $x = 0.7$, which yielded a complex multiphase mixture, indicating the end of the solid solution (see Supporting Information S3). Across the series, the lattice parameter of the garnet phase shows a clear evolution, with a systematic peak shift towards lower 2θ angle (see trend in the (420) peak position, expanded in Figure 3a) corresponding to a linear expansion of the unit cell in the range $0 \le x \le 0.60$ (Figure 3b). Based on this analysis, the compositional limit of the garnet phase in $Gd_{3+x}Al_{5-x}O_{12}$ lies close to $x = 0.60$.

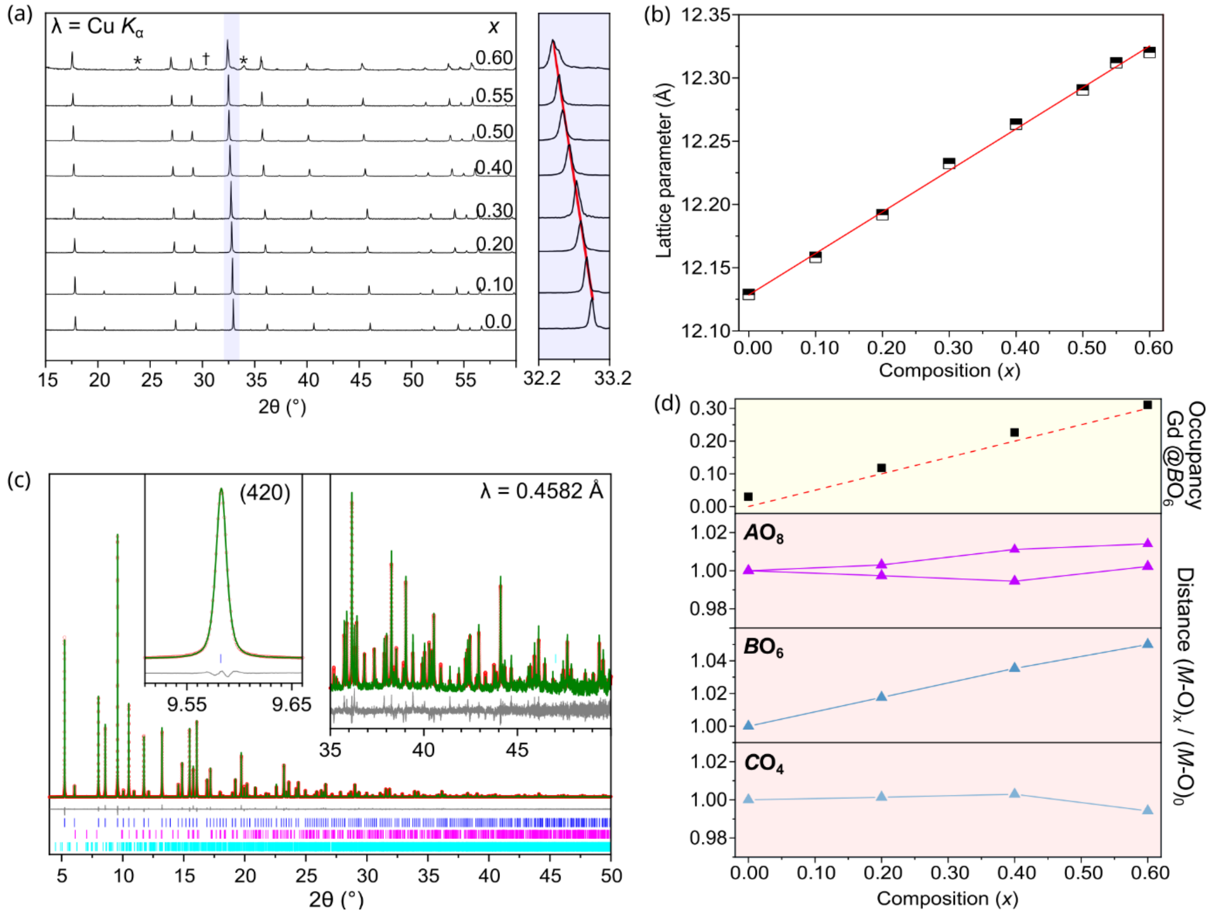

Figure 3. Structural analysis of $Gd_{3+x}Al_{5-x}O_{12}$ in the range $0 \leq x \leq 0.60$. (a) Laboratory PXRDs showing the retention of the garnet structure with a systematic shift in peak position as x increases (* = $GdAlO_3$, † = $Gd_4Al_2O_9$), and (b) the corresponding lattice parameters derived from profile fitting. (c) Rietveld fit to SXRD data from composition $x = 0.40$ (red points = y_{obs}, green line = y_{calc}, gray line = y_{obs}-y_{calc}, blue ticks = garnet, magenta ticks = 0.50(1) wt.% $GdAlO_3$, cyan ticks = 0.09(1) wt.% $Gd_4Al_2O_9$). (d) Refined structural parameters from SXRD showing fractional occupancy of Gd^{3+} at the BO_6 sites (black squares, top panel) with the nominal trend indicated by the dashed red line; and normalized metal-oxygen distances at the three different cation sites (colored triangles, lower panels).

Structural evolution and detailed structural information were analyzed by Rietveld refinement against high-resolution SPD data for the nominal compositions $x = 0$, 0.20, 0.40 and 0.60. The starting models were based on the $Gd_3Al_5O_{12}$ garnet structure for nonstoichiometric compositions ($x = 0.20$, 0.40 and 0.60). The refined models were based upon the $Y_{3+x}Al_{5-x}O_{12}$ family[10], with excess Gd^{3+} included by replacing a nominal amount of Al^{3+} at the B sublattice. The Gd^{3+}/Al^{3+} occupancy ratio at this site was then allowed to refine freely. The lattice parameter was refined, in addition to the oxygen atomic coordinates and isotropic atomic displacement parameters for each site. Figure 3c shows the refinement profile of $Gd_{3.4}Al_{4.6}O_{12}$ (see Supporting Information S13-18 for $x = 0$, 0.2 and 0.6 and refined parameters for all samples). The occupancy by Gd^{3+} of the B sublattice was found to increase linearly with x, consistent with the theoretical solid solution formula (Figure 3d, upper panel). The

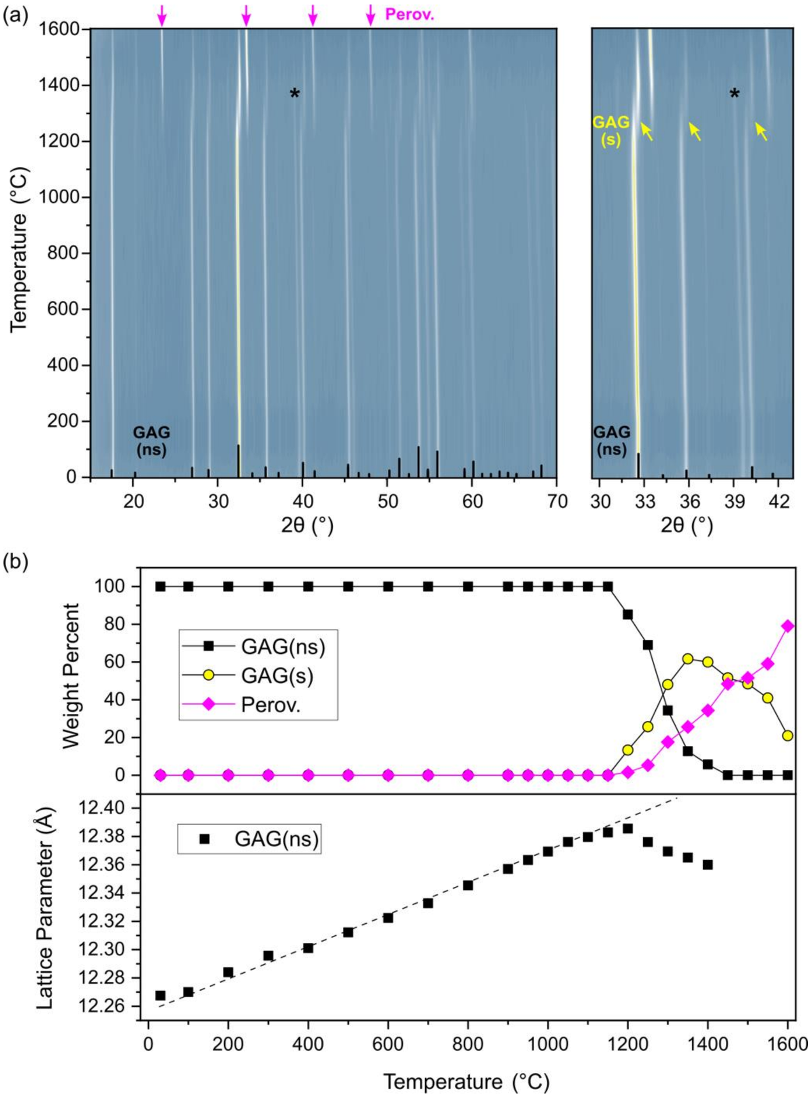

Figure 4. In-situ PXRD of $Gd_{3.4}Al_{4.6}O_{12}$ collected on heating from room temperature to 1600°C. (a) Contour plot of the region $15 \leq 2\theta \leq 70°$. Expected peaks/intensities from $Gd_{3.4}Al_{4.6}O_{12}$ "GAG(ns)" are shown by the black stick diagram at the base of the frame. Peaks due to $GdAlO_3$ "Perov." are indicated by magenta arrows at the top of the frame. The peaks corresponding to stoichiometric $Gd_3Al_5O_{12}$ "GAG(s)" are indicated by yellow arrows in the zoomed panel. Peaks from the platinum sample holder are marked by asterisks. (b) Rietveld-refined weight percentages of $Gd_{3.4}Al_{4.6}O_{12}$, $Gd_3Al_5O_{12}$ and $GdAlO_3$ as a function of temperature (top panel) and the lattice parameter evolution of $Gd_{3.4}Al_{4.6}O_{12}$ (bottom panel) showing abrupt changes at ~1200°C. The dashed line is a guide to the eye.

variations in refined *M*-O distances are shown in the lower panels of Figure 3d. A strong linear increase of the *B*-O distance with x in the range $0 \leq x \leq 0.6$ is observed, which is associated with the larger Gd^{3+}(0.94 Å) occupying the Al^{3+}(0.535 Å) at this site. At the same time, the *A*-O and *C*-O distance trends sites show a much weaker dependence with x, consistent with these sites being populated entirely by

Gd^{3+} and Al^{3+} respectively. These trends are consistent with those observed in the nonstoichiometric YAG system (Supporting Information Figure C4).

3.3 Thermal stability

The thermal stability of $Gd_{3+x}Al_{5-x}O_{12}$ was evaluated by in situ PXRD, for compositions x = 0, 0.2, 0.4 and 0.6. The nonstoichiometric members (x > 0) showed similar decomposition behaviors, exemplified by the x = 0.4 member in Figure 4 (x = 0.2 and 0.6 members are shown in Supporting Information S10-11). Here, it can be seen that the Bragg peaks shift systematically on heating from 30 – 1150°C due to thermal expansion, with garnet retained as the only crystalline phase. Between 1150 and 1200°C, two new sets of new Bragg peaks appear, indicating the onset of decomposition into perovskite $GdAlO_3$ and stoichiometric garnet $Gd_3Al_5O_{12}$, as shown in Figure 4a and the upper panel of 4b. The lattice parameter evolution of the nonstoichiometric garnet phase from RT to 1600°C is shown in Figure 4b (lower), demonstrating first a linear increase due to thermal expansion from room temperature up to ~1200°C, followed by an abrupt change in gradient associated with the onset of decomposition into $Gd_3Al_5O_{12}$ and $GdAlO_3$, which are the only observed crystalline phases at 1400°C. The decomposition onset temperature decreases slightly with increasing *x*, from 1200 – 1250°C for x = 0.2, to 1050 – 1100°C for x = 0.6. In contrast, the stoichiometric member (x = 0) is stable until 1350°C, before decomposing into $GdAlO_3$ and Al_2O_3, consistent with previous ex situ studies.[17,19]

3.4 Dopant distribution and UC properties of $(Gd_{0.89}Yb_{0.1}Tm_{0.01})_{3+x}Al_{5-x}O_{12}$

The distribution of RE^{3+} activators over two cation sublattices may have important implications for the luminescence properties[10], but very few bulk probes are adapted to this problem in $Gd_{3+x}Al_{5-x}O_{12}$. Notably, there is negligible X-ray contrast between Gd^{3+} and other RE^{3+} ions; neutron diffraction is inhibited by the presence of ^{157}Gd; and NMR techniques are inhibited by paramagnetism. However, X-ray absorption spectroscopy allows some combinations of Gd^{3+} and RE^{3+} to be studied without interference between their spectra: this is the case for $RE = Tm^{3+}$ or Yb^{3+}, whose L_3-edges are sufficiently far in energy from that of Gd^{3+} to allow them to be resolved by EXAFS.

Three series $Gd_{3+x}Al_{5-x}O_{12}$, $(Gd_{0.9}Tm_{0.1})_{3+x}Al_{5-x}O_{12}$ and $(Gd_{0.9}Yb_{0.1})_{3+x}Al_{5-x}O_{12}$ were prepared with $x = 0$, 0.2 and 0.4, and their EXAFS spectra were recorded at the Gd, Tm and Yb L_3 edges. The first coordination sphere Gd-O and Tm(Yb)-O distances were extracted from fits to the EXAFS spectra, and these were compared with theoretical *M*-O distances calculated by DFT relaxation of 1 x 1 x 1 garnet cells (see *Methods*). The experimental and theoretical *M*-O distances are plotted together in Figure 5, and the corresponding EXAFS fits and DFT-relaxed models are shown in Supporting Information S19-23. For the Tm^{3+} and Yb^{3+} doped series, two opposing scenarios are considered: Scenario 1, where Tm^{3+} or Yb^{3+} populate only the AO_8 sites (displacing Gd^{3+} to the BO_6 sublattice when $x > 0$), and Scenario 2 which maximises the population of Tm^{3+} or Yb^{3+} at the BO_6 sites (Figure 5a). These two scenarios give very different expected trends in (Tm, Yb)-O distance (Figure 5c), either negligible change with *x* (Scenario 1) or a strong decrease followed by a plateau at higher *x* values when the number of available *B* sites becomes greater than the number of (Tm, Yb) ions (Scenario 2). The corresponding experimental data show decreasing trends for both Tm-O and Yb-O distance with *x*, with a similar magnitude to that predicted for Scenario 2 (Figure 5d, e). This indicates that Tm and Yb both tend to occupy the BO_6 sites in $(Gd_{0.9}RE_{0.1})_{3+x}Al_{5-x}O_{12}$ when $x > 0$. The weak variation of Gd-O distance with *x* in both scenarios is consistent with the undoped $Gd_{3+x}Al_{5-x}O_{12}$ series, where the prevailing lattice parameter increase is countered by an increasing population of octahedral Gd^{3+} (see Supporting Information S23).

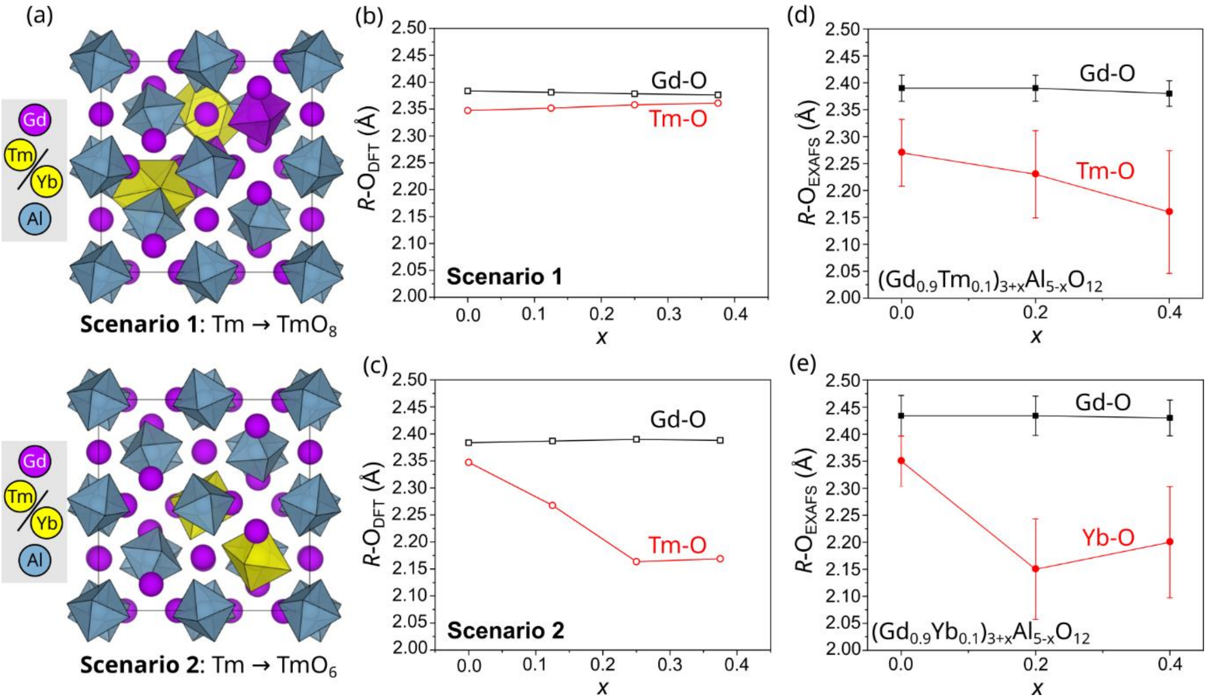

Figure 5. Site preferences of Tm^{3+} and Yb^{3+} dopants by EXAFS and DFT (a) Two representative unit cells relaxed by DFT, from Scenario 1 (Tm/Yb^{3+} populates *A* sites) and Scenario 2 (Tm/Yb^{3+} populates *B* sites) respectively, both with $x = 0.25$. The *C* sites are omitted for clarity. (b, c) DFT-calculated trends in Gd-O and Tm-O distances, according to Scenario 1 and Scenario 2. (d, e) Experimental trends in *R*-O distances (*R* = Gd, Tm or Yb) derived from EXAFS spectra, exhibiting Scenario 2-like behavior.

Powder samples of $(Gd_{0.89}Tm_{0.01}Yb_{0.10})_{3+x}Al_{5-x}O_{12}$ with x = 0, 0.2 and 0.4 were prepared by the same protocol as for the parent $Gd_{3+x}Al_{5-x}O_{12}$ series, and confirmed to crystallize into the garnet structure by PXRD (Supporting Information S24). Bead samples were then prepared for the same compositions and polished into disks of ~2mm diameter for luminescence measurements. Electron microprobe analysis of the disks (Supporting Information S25-28) showed a homogeneous distribution of Gd, Tm and Yb at the micron scale. The normalized UC responses of these samples under 980 nm excitation are shown in Figure 6a. Here, the near-IR emission band arising from the $^1G_4$-$^3H_5$/$^3H_4$-$^3H_6$ transition of Tm^{3+} (region 720 – 820 nm) shows marked changes in fine structure with increasing x, with the most intense emission peaks in x = 0.2 and x = 0.4 located at 806 nm and 795 nm, rather than 783 nm for x = 0. The

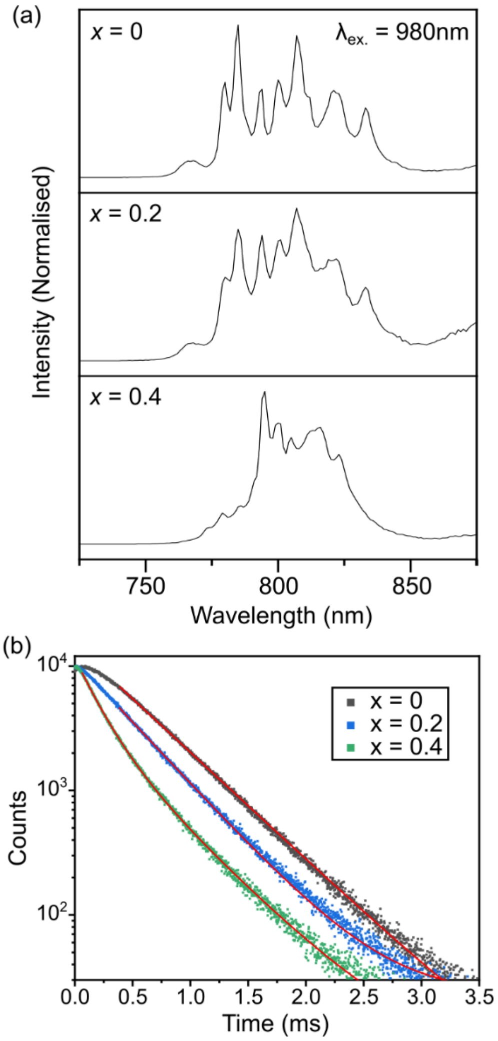

Figure 6. (a) Upconversion emission spectra of single beads of $(Gd_{0.89}Tm_{0.01}Yb_{0.10})_{3+x}Al_{5-x}O_{12}$ for x = 0, 0.2 and 0.4 in the near-infrared, using an exitation wavelength of 980 nm. (b) Luminescence decay curves of the 780 nm emission line, with single- (x = 0, 0.2) or double- (x = 0.4) exponential fits overlaid in red.

x = 0.4 spectrum is strongly modified with respect to the x = 0 and 0.2 spectra, with a marked collapse in the intensity of the 783 nm emission line. This may reflect a switch from a regime where (Tm^{3+}, Yb^{3+}) are distributed between the *A*- and *B*-sublattices, to one where they can be accommodated at the *B*-sublattice only (see Discussion, Section 4). At the same time, the luminescence lifetimes (measured at 780 nm) are progressively shortened as nonstoichiometry increases (Figure 6b). The emission mechanism does not vary with nonstoichiometry, with all compositions exhibiting a two-electron transfer process determined by measurements of luminescence intensity vs pump power (Figure E5). These behaviors are qualitatively similar to those of the nonstoichiometric YAG:(Er^{3+}, Yb^{3+}) upconversion phosphors[10].

3.5 Nonstoichiometric $(Gd_{0.98}Ce_{0.02})_{3+x}Al_{5-x}O_{12}$ and $(Gd_{0.9}Tb_{0.1})_{3+x}Al_{5-x}O_{12}$ phosphors

To explore the response of other classes of phosphor to nonstoichiometry, we prepared two representative systems showing (i) broad-band emission by Ce^{3+} doping $(Gd_{0.98}Ce_{0.02})_{3+x}Al_{5-x}O_{12}$ and (ii) narrow-band emission by Tb^{3+} doping $(Gd_{0.9}Tb_{0.1})_{3+x}Al_{5-x}O_{12}$. In contrast with the Tm/Yb upconversion system, and due to the difficulties in contrasting Gd^{3+} and other RE^{3+} ions by different techniques (see Section 3.4), the luminescence responses of these phosphors are presented here without precise experimentally-determined information on the dopant distribution within the crystal structures (although atomic scale STEM-EDS data do suggest an unquantified amount of Tb^{3+} at the BO_6 sites in $(Gd_{0.9}Tb_{0.1})_{3.4}Al_{4.6}O_{12}$ – see Supporting Information S35-37). The emission spectra and luminescence lifetimes of the Ce^{3+} and Tb^{3+} phosphors are shown together in Figure 7, and their structural and compositional analyses are detailed in Supporting Information sections S31-34 and S35-37 respectively.

In $(Gd_{0.98}Ce_{0.02})_{3+x}Al_{5-x}O_{12}$, the main emission line centered at ~600 nm undergoes a slight broadening with an associated red-shift as nonstoichiometry (x) increases. At the same time, its luminescence lifetimes decrease, with average decay times of 49, 35 and 31 ns for x = 0, 0.2 and 0.4 respectively. These trends are very similar to those exhibited by nonstoichiometric YAG:Ce^{3+}, where Ce^{3+} populates the AO_8 sublattice only, and the line broadening is ascribed to increasing disorder in the second coordination sphere of Ce^{3+}. In contrast, the PL spectra and lifetimes of the narrow-band $(Gd_{0.9}Tb_{0.1})_{3+x}Al_{5-x}O_{12}$ phosphors are essentially insensitive to nonstoichiometry, representing typical behavior for this class of activator.

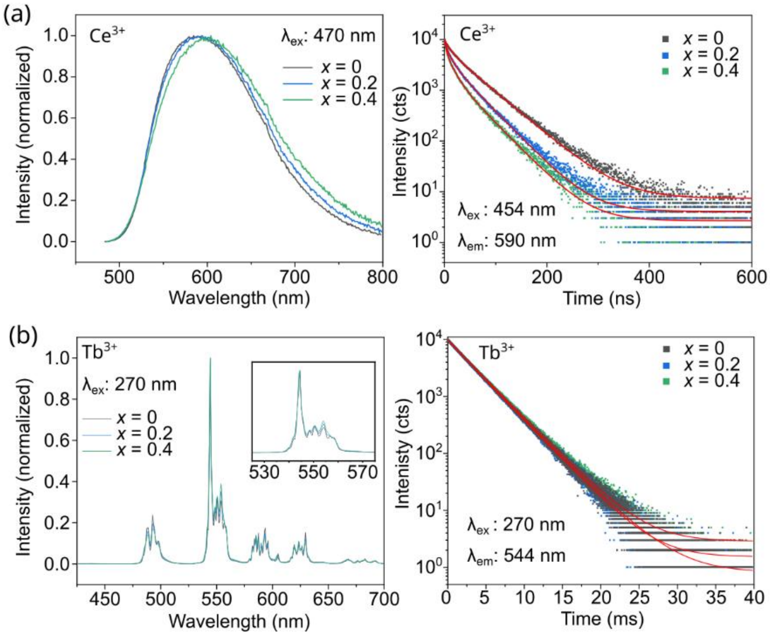

Figure 7. Luminescence properties of some other nonstoichiometric phosphor types. (a,b) PL of $(Gd_{0.98}Ce_{0.02})_{3+x}Al_{5-x}O_{12}$ and $(Gd_{0.9}Tb_{0.1})_{3+x}Al_{5-x}O_{12}$ with $x = 0$, 0.2 and 0.4 excited at 470 nm and 270 nm respectively, shown together with their lifetimes (fits overlaid in red).

4. Discussion

The compositional range established here for gadolinium aluminate garnet is extraordinary. At its extreme, the composition $Gd_{3.6}Al_{4.4}O_{12}$ (Gd/Al = 0.82) is closer to the adjacent perovskite phase $GdAlO_3$ (Gd/Al = 1) than it is to its parent garnet phase $Gd_3Al_5O_{12}$ (Gd/Al = 0.6). Rare-earth aluminates have long been considered to behave as line phases, and major departures from this behaviour (e.g. $x > 0.03$) have only recently been demonstrated in the analogous YAG system (stable up to $x = 0.4$)[10]. In the related rare-earth gallate garnets $RE_{3+x}Ga_{5-x}O_{12}$, nonstoichiometries of a similar magnitude have very recently been reported with $x < 0.2$ (for $RE = Gd^{3+}$) and $x < 0.6$ (for the smallest rare-earth members Er, Yb and Lu)[30,31] by conventional ceramic synthesis, but nonstoichiometric aluminates could not be made by this synthesis route: these are summarized in the Supporting Information (S38 – 39). By a simple ionic radius argument, the $Gd_{3+x}Al_{5-x}O_{12}$ (GAG) solid solution is expected to be less amenable than YAG or $Gd_{3+x}Ga_{5-x}O_{12}$ (GGG) to this type of nonstoichiometry. YAG and GGG have ionic radius ratios r_A/r_B of 1.68 and 1.51 respectively (using ionic radii of 6-coordinated Y^{3+}, Gd^{3+} and Ga^{3+}),[32] but GAG has the greatest size mis-match between *A* and *B* cations with $r_{Gd}/r_{Al} = 1.75$. Indeed, compared to YAG, the nonstoichiometric GAG system exhibits a more pronounced volume expansion with increasing x because Gd^{3+} is larger than Y^{3+}, as shown in Figure S16.

The location of the compositional limit $x = 0.6$ at the half-way point between the ideal stoichiometries of garnet and perovskite is probably not coincidental, and may reflect strongly increasing competition from the crystallization of other stable phases which are closer in composition (notably ABO_3-type phases). It is notable that a similar limit ($x \approx 0.5$) is reported in the highly nonstoichiometric small-rare-earth gallate garnets[30]. In contrast, nonstoichiometry in the $Y_{3+x}Al_{5-x}O_{12}$ system appears to be limited by the extent of the $Y_2O_3 - Al_2O_3$ glass-forming domain (at $x = 0.4$), rather than the proximity of competing phases. This also suggests that the local atomic arrangements in the precursor glasses (composed mainly of AlO_4 and AlO_5 species at $x = 0$)[33] have an important role in phase selection, offering a more facile route to the crystallization of garnets (where at least 60% of Al^{3+} is in tetrahedral coordination) than to perovskites (where Al^{3+} is exclusively in octahedral coordination). Together, these factors should work to define the compositional limits for different RE^{3+} across the 4*f* series: for each RE^{3+}, the accessible nonstoichiometric range should depend on the preparation of a suitable activated precursor of the desired composition (glass, or other types such as a solution-derived precursor), up to an intrinsic limit of $x \approx 0.6$. In addition to the interest of such materials for optical properties (discussed below), this could also open a new range of compounds of interest for their low temperature magnetic or magnetocaloric properties.[10,11,30,31]

The measurement of the PL spectra of several nonstoichiometric GAG phosphor types, along with previous study of the nonstoichiometric YAG system, allows a general picture to emerge about the luminescence responses of this materials class. It is the case in both GAG and YAG that upconversion phosphors are most strongly affected by increasing nonstoichiometry. In both examples, these phosphors follow complex emission schemes (two-photon absorption), contain small rare-earth activators (Er^{3+} or Tm^{3+}) that populate two cation sublattices in the host material, and a high concentration of small rare-earth sensitizer (Yb^{3+}) with a similar crystallographic distribution to the activators. The nonstoichiometric YAG-based upconversion phosphors were previously studied to a limit of $x = 0.2$ and their spectra showed an approximately linear evolution with x.[10] Here, the behaviour of $(Gd_{0.89}Tm_{0.01}Yb_{0.1})_{3+x}Al_{5-x}O_{12}$ over a more extended range $0 \leq x \leq 0.4$, indicates that this evolution will not necessarily remain linear as x increases to very high values, possibly due to different local configurations that can arise at such compositions. For example, the collapse in intensity of the 780 nm emission line between $x = 0.2$ and 0.4 (Figure 6a) coincides with a crossover-point where the number of Al^{3+} ions removed from the *B* sublattice becomes larger than the number of dopant (Tb^{3+}, Yb^{3+}) ions (see Supporting Information S29), permitting configurations with the optically-active species accommodated exclusively at the *B* sublattice. In-depth studies at low temperature may help to unravel the physical origin of the spectral changes observed here, for example a relaxation of selection rules to favor emission from electric dipole transitions (such as $^1G_4$-$^4H_5$) over magnetic dipole transitions (such as $^3H_4$-$^3H_6$).[34] The exploration of other $RE_{3+x}Al_{5-x}O_{12}$ systems may help to clarify such links between crystal chemistry and luminescence properties, and may be expected to yield a significant number of new modified upconversion phosphors.

In both GAG and YAG the Ce^{3+} phosphors are only weakly perturbed by nonstoichiometry, associated with Ce^{3+} retaining an 8-fold first-coordination sphere (shown experimentally for nonstoichiometric YAG:Ce^{3+}). The PL response of Ce^{3+} is highly sensitive to its local coordination environment, and the incorporation of significant concentrations of Ce^{3+} at the BO_6 sublattice might be expected to produce strong changes in emission properties. Strategies to achieve this may include development of highly nonstoichiometric $Eu_{3+x}Al_{5-x}O_{12}$:Ce^{3+} hosts. In such a system, the smaller ionic size contrast between Eu^{3+} and Ce^{3+} may help to homogenize their distribution between *A* and *B* sites. Finally, whilst the indifference of the narrow-band emitter Tb^{3+} to nonstoichiometry suggests that there is little interest in pursuing other highly nonstoichiometric phosphors of this type, there is scope for other types of nonstoichiometric phosphor (beyond those reported here) to be developed, for example in $Gd_3Al_5O_{12}$ – $Gd_3Ga_5O_{12}$ (GAG-GGG) solid solutions which are an important class of persistent luminescence host.[8,35]

5. Conclusions

The crystallization of glass precursors at a moderate temperature of 950°C can be used to isolate highly nonstoichiometric gadolinium aluminate garnets $Gd_{3+x}Al_{5-x}O_{12}$ with $0 \le x \le 0.60$, which are described here for the first time. Once formed, these materials are highly stable, with composition-dependent thermal decomposition temperatures in the range 1050 – 1200°C. Despite the major size contrast between the two cation species, the garnet structure accommodates excess Gd^{3+} by replacement of

Al^{3+} at the octahedral BO_6 sublattice: 30% of these sites are occupied by Gd^{3+} in the end-member $Gd_{3.6}Al_{4.4}O_{12}$. The nonstoichiometric range is more extensive than the analogous $Y_{3+x}Al_{5-x}O_{12}$ system ($0 \leq x \leq 0.4$) due to a broader glass-forming domain in the Gd_2O_3 – Al_2O_3 binary system, with the compositional limit of $x = 0.6$ lying half-way between ideal garnet and perovskite stoichiometries. In common with the nonstoichiometric YAG system, nonstoichiometry has a marked effect on upconversion emission phosphors where dopants can occupy two cation sublattices (AO_8 and BO_6), demonstrated here in the Tm/Yb-substituted system $(Gd_{0.89}Yb_{0.1}Tm_{0.01})_{3+x}Al_{5-x}O_{12}$. This implies that the exploration of other nonstoichiometric $RE_{3+x}Al_{5-x}O_{12}$ hosts may be particularly interesting for the development of new upconversion systems with small rare-earth dopants, as well as yet-unexplored applications in persistent luminescence and magnetism.

Supporting Information

Aerodynamic levitator details; DSC; PXRD; Rietveld analysis; EXAFS analysis; SEM imaging; electron microprobe; HAADF-STEM imaging; STEM-EDS analysis; luminescence

Acknowledgements

Funding was provided by the French National Research Agency (ANR) under projects 20-CE08-0007 CAPRE and ANR-23-CE08-0013-01 HighFive, and by the I + D + I Grant PID2021-122328OB-I00 funded by MCIN/AEI/10.13039/501100011033 and by “ERDF A way of making Europe”. Electron microscopy facilities were provided by the Platform MACLE - CVL, co-funded by the European Union and the Centre-Val de Loire Region (FEDER). Xue Fang acknowledges the China Scholarship Council (CSC) for a PhD scholarship (project 202008450026). Victor Castaing thanks Junta de Andalucía for financial support (POSTDOC_21_00694). Use of the Advanced Photon Source at Argonne National Laboratory was supported by the U. S. Department of Energy, Office of Science, Office of Basic Energy Sciences, under Contract No. DE-AC02-06CH11357. This work used the Cirrus UK National Tier-2 HPC Service at EPCC (http://www.cirrus.ac.uk) funded by the University of Edinburgh and EPSRC (EP/P020267/1). Access to the SAMBA beamline (SOLEIL synchrotron, Gif-sur-Yvette, France) was granted under proposal 20211197. We thank Dr. Emiliano Fonda for assistance with EXAFS data collection, Sandra Ory (CEMHTI, Orléans) for DSC measurements and TEM sample preparation, and Pierre-Loup Savary (CEMHTI, Orléans) for preparation of additional glass precursors.

References

(1) Geusic, J. E.; Marcos, H. M.; Van Uitert, L. G. Laser Oscillations in Nd-Doped Yttrium Aluminum, Yttrium Gallium and Gadolinium Garnets. *Applied Physics Letters* **1964**, *4* (10), 182–184.

(2) Ye, S.; Xiao, F.; Pan, Y. X.; Ma, Y. Y.; Zhang, Q. Y. Phosphors in Phosphor-Converted White Light-Emitting Diodes: Recent Advances in Materials, Techniques and Properties. *Materials Science and Engineering R: Reports* **2010**, *71* (1), 1–34.

(3) Nikl, M.; Yoshikawa, A. Recent R&D Trends in Inorganic Single-Crystal Scintillator Materials for Radiation Detection. *Advanced Optical Materials* **2015**, *3* (4), 463–481.

(4) Lafargue-Dit-Hauret, W.; Allix, M.; Viana, B.; Jobic, S.; Latouche, C. Computational Analysis on Native and Extrinsic Point Defects in YAG Using the metaGGA SCAN Method. *Theor Chem Acc* **2022**, *141* (10), 58.

(5) Patel, A. P.; Levy, M. R.; Grimes, R. W.; Gaume, R. M.; Feigelson, R. S.; McClellan, K. J.; Stanek, C. R. Mechanisms of Nonstoichiometry in $Y_3Al_5O_{12}$. *Applied Physics Letters* **2008**, *93* (19), 191902.

(6) Patel, A. P.; Stanek, C. R.; Grimes, R. W. Comparison of Defect Processes in REAlO3 Perovskites and $RE_3Al_5O_{12}$ Garnets. *physica status solidi (b)* **2013**, *250* (8), 1624–1631.

(7) Cao, W.; Becerro, A. I.; Castaing, V.; Fang, X.; Florian, P.; Fayon, F.; Zanghi, D.; Veron, E.; Zandonà, A.; Genevois, C.; Pitcher, M. J.; Allix, M. Highly Nonstoichiometric YAG Ceramics with Modified Luminescence Properties. *Adv. Funct. Mater.* **2023**, *33*, 2213418.

(8) Xu, J.; Ueda, J.; Tanabe, S. Design of Deep-Red Persistent Phosphors of $Gd_3Al_{5-x}Ga_xO_{12}$:Cr^{3+} Transparent Ceramics Sensitized by Eu^{3+} as an Electron Trap Using Conduction Band Engineering. *Opt. Mater. Express, OME* **2015**, *5* (5), 963–968.

(9) Tomala, R.; Korkus, K.; Boiko, V.; Hreniak, D.; Głuchowski, P. Electronic Structure Engineering of $Gd_{2.97}Tb_{0.03}Ga_{5-x}Al_xO_{12}$ Persistent Luminescence Phosphors. *Journal of Alloys and Compounds* **2021**, *889*, 161745.

(10) Florea, O.; Lhotel, E.; Jacobsen, H.; Knee, C. S.; Deen, P. P. Absence of Magnetic Ordering and Field-Induced Phase Diagram in the Gadolinium Aluminum Garnet. *Phys. Rev. B* **2017**, *96* (22), 220413.

(11) Sackville Hamilton, A. C.; Lampronti, G. I.; Rowley, S. E.; Dutton, S. E. Enhancement of the Magnetocaloric Effect Driven by Changes in the Crystal Structure of Al-Doped GGG, $Gd_3Ga_{5-x}Al_xO_{12}$ ($0 \leq x \leq 5$). *Journal of Physics Condensed Matter* **2014**, *26* (11), 116001.

(12) Lin, H.; Zhou, S.; Teng, H. Synthesis of $Tb_3Al_5O_{12}$ (TAG) Transparent Ceramics for Potential Magneto-Optical Applications. *Optical Materials* **2011**, *33* (11), 1833–1836.

(13) Li, J.-G.; Sakka, Y. Recent Progress in Advanced Optical Materials Based on Gadolinium Aluminate Garnet ($Gd_3Al_5O_{12}$). *Science and Technology of Advanced Materials* **2015**, *16* (1), 014902.

(14) Liu, G.; Wang, B.; Li, J.; Cao, B.; Lu, Y.; Liu, Z. Research Progress of Gadolinium Aluminum Garnet Based Optical Materials. *Physica B: Condensed Matter* **2021**, *603*, 412775.

(15) Wu, P.; Pelton, A. D. Coupled Thermodynamic-Phase Diagram Assessment of the Rare Earth Oxide-Aluminium Oxide Binary Systems. *Journal of Alloys and Compounds* **1992**, *179* (1–2), 259–287.

(16) Garskaite, E.; Dubnikova, N.; Katelnikovas, A.; Pinkas, J.; Kareiva, A. Syntheses and Characterisation of $Gd_3Al_5O_{12}$ and $La_3Al_5O_{12}$ Garnets. *Collect. Czech. Chem. Commun.* **2007**, *72* (3), 321–333.

(17) Shishido, T.; Okamura, K.; Yajima, S. Gd3Al5O12 Phase Obtained by Crystallization of Amorphous $Gd_2O_3 \cdot 5/3Al_2O_3$. *Journal of the American Ceramic Society* **1978**, *61* (7–8), 373–375.

(18) Tang, J.; Gou, J.; Li, G.; Li, Y.; He, H.; Li, C.; Yang, J. Synthesis, Structure and Upconversion Luminescence of Yb^{3+}, Ho^{3+} Co-Doped $Gd_3Al_5O_{12}$ Garnet Phosphor Prepared by the Pechini Sol–Gel Method. *RSC Adv.* **2016**, *6* (59), 54435–54439.

(19) Li, J.; Li, J.-G.; Zhang, Z.; Wu, X.; Liu, S.; Li, X.; Sun, X.; Sakka, Y. Gadolinium Aluminate Garnet ($Gd_3Al_5O_{12}$): Crystal Structure Stabilization via Lutetium Doping and Properties of the $(Gd_{1-x}Lu_x)_3Al_5O_{12}$ Solid Solutions (x = 0–0.5). *Journal of the American Ceramic Society* **2012**, *95* (3), 931–936.

(20) Garskaite, E.; Sakirzanovas, S.; Kareiva, A.; Glaser, J.; Meyer, H. J. Synthesis and Structure of Europium Aluminium Garnet (EAG). *Z. Anorg. Allg. Chem.* **2007**, *633* (7), 990–993.

(21) Coelho, A. A. TOPAS and TOPAS-Academic: An Optimization Program Integrating Computer Algebra and Crystallographic Objects Written in C++: An. *J. Appl. Crystallogr.* **2018**, *51* (1), 210–218.

(22) Alain, M.; Jacques, M.; Diane, M. B.; Karine, P. MAX: Multiplatform Applications for XAFS. *Journal of Physics: Conference Series* **2009**, *190* (1), 012034.

(23) *https://www.synchrotron-soleil.fr/en/beamlines/samba*. Accessed 30/5/2024.

(24) Ankudinov, A.; Ravel, B.; Rehr, J. J.; Conradson, S. D. Real-Space Multiple-Scattering Calculation and Interpretation of x-Ray-Absorption near-Edge Structure. *Physical Review B - Condensed Matter and Materials Physics* **1998**, *58* (12), 7565–7576.

(25) Okhotnikov, K.; Charpentier, T.; Cadars, S. Supercell Program: A Combinatorial Structure-Generation Approach for the Local-Level Modeling of Atomic Substitutions and Partial Occupancies in Crystals. *Journal of Cheminformatics 2016 8:1* **2016**, *8* (1), 1–15.

(26) Kresse, G.; Furthmüller, J. Efficient Iterative Schemes for Ab Initio Total-Energy Calculations Using a Plane-Wave Basis Set. *Phys. Rev. B* **1996**, *54* (16), 11169–11186.

(27) Perdew, J. P.; Ruzsinszky, A.; Csonka, G. I.; Vydrov, O. A.; Scuseria, G. E.; Constantin, L. A.; Zhou, X.; Burke, K. Restoring the Density-Gradient Expansion for Exchange in Solids and Surfaces. *Phys. Rev. Lett.* **2008**, *100* (13), 136406.

(28) Kresse, G.; Joubert, D. From Ultrasoft Pseudopotentials to the Projector Augmented-Wave Method. *Phys. Rev. B* **1999**, *59* (3), 1758.

(29) Ma, X.; Li, X.; Li, J.; Genevois, C.; Ma, B.; Etienne, A.; Wan, C.; Véron, E.; Peng, Z.; Allix, M. Pressureless Glass Crystallization of Transparent Yttrium Aluminum Garnet-Based Nanoceramics. *Nature Communications* **2018**, *9* (1), 1175.

(30) Yang, C.; Jin, L.; Xie, W.; Cava, R. J. Stuffed Rare-Earth Garnets. *Inorg. Chem.* **2023**, *62* (51), 21364–21370.

(31) Yang, C.; Wang, H.; Jin, L.; Xu, X.; Ni, D.; Thompson, J. D.; Xie, W.; Cava, R. J. Erbium-Excess Gallium Garnets. *Inorg. Chem.* **2023**, *62* (34), 13731–13737.

(32) Shannon, R. D. Revised Effective Ionic Radii and Systematic Studies of Interatomic Distances in Halides and Chalcogenides. *Acta Cryst A* **1976**, *32* (5), 751–767.

(33) Florian, P.; Gervais, M.; Douy, A.; Massiot, D.; Coutures, J.-P. A Multi-Nuclear Multiple-Field Nuclear Magnetic Resonance Study of the Y_2O_3–Al_2O_3 Phase Diagram. *J. Phys. Chem. B* **2001**, *105* (2), 379–391.

(34) Dodson, C. M.; Kurvits, J. A.; Li, D.; Jiang, M.; Zia, R. Magnetic Dipole Emission of Dy^{3+}:Y_2O_3 and Tm^{3+}:Y_2O_3 at near-Infrared Wavelengths. *Opt. Mater. Express, OME* **2014**, *4* (11), 2441–2450.

(35) Castaing, V.; Lozano, G.; Míguez, H. Transparent Phosphor Thin Films Based on Rare-Earth-Doped Garnets: Building Blocks for Versatile Persistent Luminescence Materials. *Advanced Photonics Research* **2022**, *3* (7), 2100367.